Grid Cell Percolation

Yuri Dabaghian
Yuri.A.Dabaghian@uth.tmc.edu
Department of Neurology, University of Texas McGovern Medical School, Houston,
TX 77030, U.S.A.

Grid cells play a principal role in enabling cognitive representations of ambient environments. The key property of these cells—the regular arrangement of their firing fields—is commonly viewed as a means for establishing spatial scales or encoding specific locations. However, using grid cells' spiking outputs for deducing geometric orderliness proves to be a strenuous task due to fairly irregular activation patterns triggered by the animal's sporadic visits to the grid fields. This article addresses statistical mechanisms enabling emergent regularity of grid cell firing activity from the perspective of percolation theory. Using percolation phenomena for modeling the effect of the rat's moves through the lattices of firing fields sheds new light on the mechanisms of spatial information processing, spatial learning, path integration, and establishing spatial metrics. It is also shown that physiological parameters required for spiking percolation match the experimental range, including the characteristic 2/3 ratio between the grid fields' size and the grid spacing, pointing at a biological viability of the approach.

1 Introduction

Cognitive representation of space is sustained by the spiking activity of "spatially tuned" neurons, such as hippocampal place cells, head direction cells, parietal cells, and border cells (Moser & Kropff, 2008; Grieves & Jeffery, 2017). A particularly curious pattern of activity is exhibited by the grid cells in the rats' medial entorhinal cortex (MEC) that fire in compact domains centered at the vertices of a triangular lattice, tiling the navigated environment (Hafting et al., 2005; see Figure 1A). The exact principles by which these cells contribute to spatial awareness remain a matter of debate. It is commonly assumed that MEC outputs are used to represent the animal's ongoing location and to establish global spatial metrics (Bush et al., 2015; Moser & Moser, 2008; Fiete et al., 2008; Welinder et al., 2008). However, extracting these structures from the spike train patterns is a complex task: since the animal can visit one firing field at a time, the sequences of grid cell responses depend on the shape of the rat's trajectory and can be highly intermittent. In the absence of simple universal decoding algorithms, the
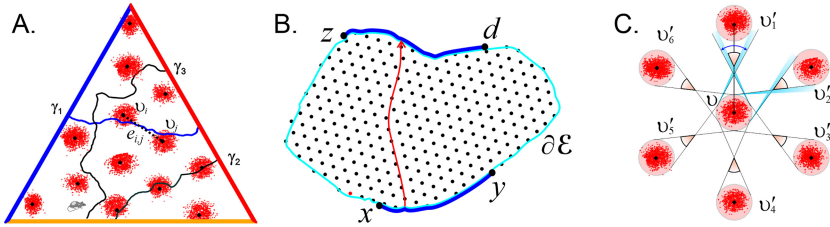
Figure 1: Grid cells. (A) Grid fields form a hexagonal lattice embedded into a 3×3 m triangular enclosure. Vertices of the lattice are shown by black dots. The diameter of each field is comparable to the animal's body size. Three curves, γ_1, γ_2, and γ_3, represent segments of paths extending from one side of a triangular environment to another. The path γ_1 crosses the grid fields v_i and v_j, eliciting spikes in both, thus opening the vertices v_i and v_j and instantiating the edge e_{ij} between them (dashed line). Path γ_2 percolates through the grid fields in sequence, without omissions, and γ_3 avoids grid fields. (B) A percolation theory setup: A path extending from one side of a lattice domain $V_{\mathcal{E}}$; that is, a boundary segment ($[a, b] \in \partial\mathcal{E}$) to another ($[z, d] \in \partial\mathcal{E}$) may open vertices or edges with fixed probabilities p_v and p_e. (C) The range of directions that lead from a grid field v to its six immediate neighbors, $v_1, \ldots, v_6$, are in pink. Directions along which a straight line escapes between the fields are in blue. For $\xi_g = 1/2$, the escape directions disappear.

effect produced by the grid cells in the downstream networks may depend primarily on activation frequency: persistently firing cells contribute most, while the ones that activate sporadically produce smaller impacts (Buzsáki, 2010). The maximal frequency of a given grid cell's responses is achieved over periods when the animal runs through its firing fields in sequence, without omissions (see Figure 1A). Under which conditions such contiguous firing can be produced in a given environment and how common are relevant questions the regularly firing cells are questions for discussion.

Curiously, these questions are reminiscent of the problems addressed in percolation theory, which describes the propagation of diffusive substances (liquids or gasses) through porous media. The key question addressed by the theory is whether a permeable domain $\mathcal{E}$ allows diffusive leaks from one side of its boundary to another (Grimmet, 1999), that is, whether the trickling through the pores can form uninterrupted sequences connecting the opposite sides, or *percolate*,[1] through, $\mathcal{E}$.

Of particular interest for the discussion in this article are mathematical models of percolation, in which physical media are represented by a segment of a regular lattice V enclosed within a domain $\mathcal{E}$. Depending on the setup, either the vertices v or the edges e of the lattice $V_{\mathcal{E}}$ represent the

_____

[1]Throughout the text, terminological definitions are given in italics.

leaking pores, which may "open" or "close" with some fixed probabilities (Grimmet, 1999; Kesten, 1982; see Figure 1B). A key result of the theory is that once these probabilities exceed certain critical thresholds (for triangular lattices, $p_v^* = 0.5$ for the vertices and $p_e^* = 2\sin(\pi/18) \approx 0.35$ for the edges), the system transitions into a *percolating phase*, in which long, uninterrupted sequences of open sites become statistically common (Wierman, 1981).

The analogy with the grid cells can be formalized as follows. Consider a triangular lattice $V_{\mathcal{E}}^g$ with vertices centered at the firing fields of a cell g. A vertex v_i^g opens if the cell g fires at the corresponding field $v_i^g = v(v_i^g)$. If the rat runs consecutively through two neighboring fields, for example, from v_i^g to v_j^g on Figure 1A, eliciting spikes in both, then the edge e_{ij}^g between them also opens. If a path γ induces a sequence of conjoint open edges,

$$\mathsf{G}_g(\gamma) = \{e_{i_1 i_2}^g, e_{i_2 i_3}^g, \ldots, e_{v_{i-1} i_k}^g\} \tag{1.1}$$

(and hence runs through a series of open sites $v_{i_1}^g, v_{i_2}^g, \ldots, v_{i_k}^g$), it will be said to percolate g. The spiking pattern of a cell g triggered by the rat's moves can then be approximated by a sequence of open vertices and edges, that is, represented by discretized the path (see equation 1.1).

As it turns out, for the experimentally observed range of firing parameters, a certain fraction of paths extending through the navigated environments percolates grid cell groups, which may then play a particular role in representing spatial information. The activity of MEC network can hence be studied from the perspective of identifying such high-impact cells, understanding their role in representing the navigated paths, and testing whether the parameters required for percolation are physiologically viable, and so forth.

2 Methods

2.1 Preliminary Estimates. Grid cell percolation depends on the probability with which a generic trajectory runs into the grid fields and the probability of eliciting spiking responses. The former is controlled by the ratio between the field size D_g and the grid spacing a_g,

$$\xi_g = D_g/a_g, \tag{2.1}$$

while the latter depends on the maximal firing rate A_g and the animal's speed s.

Lattice parameter ξ_g defines the range of directions that lead from a grid field to one of its immediate neighbors. If the gap between fields is wider than the field size, $\xi_g < 1/2$, then a finite fraction of straight directions originating at a given grid field form "escape corridors"—passageways in between the surrounding fields (see Figure 1C). At $\xi_g = 1/2$, such directions

disappear, suggesting that $\xi_g \gtrsim 1/2$ is required for enforcing the percolation. However, this requirement must be strengthened further, for two reasons. First, the trajectory cannot not just brush on the field's side, where the firing rate is too small; it should pass sufficiently close to the center to induce reliable spiking responses. Second, the empirical size of a field is defined by the lengths of the typical paths that run though it rather than the abstracted field diameter. A simple correction to equation 2.1 can hence be obtained by replacing the diameter D_g with the length of an average chord cutting through the field, $\bar{l}_g = \pi D_g / 4$ (Kellerer, 1971; Coleman, 1969), which yields $\xi_g \gtrsim 2/\pi$ (see Figure 1B).

If ξ_g grows more, the angular domains leading from field to field begin to overlap. To maintain the unambiguity of representation, the lattice parameter, equation 2.1, should remain close to the marginal value,

$$\xi_g^* \approx 2/\pi, \tag{2.2}$$

which matches the experimentally observed "isometric relation" (Hafting et al., 2005; Neher et al., 2017).

The opening probabilities on a grid field lattice depend on the parameters of neuronal activity and the animal's moves. If the maximal spiking rate of a cell g is A_g, then the mean rate is

$$\bar{\lambda}_g = C\frac{A_g D_g}{\bar{s}}, \tag{2.3}$$

where $C \approx 0.06$ is a geometric coefficient and $\bar{s}$ is the mean traversal speed (see section A.3). Experimentally, the grid field sizes sampled along the ventro-dorsal axis of MEC ranged, in smaller environments, from about 10 cm to about 20 cm (Hafting et al., 2005; Stensola et al., 2012), while the mean rates co-vary between $A_g \approx 21$ Hz and $A_g \approx 11$ Hz (i.e., the product $A_g D_g$ tends to increase as the field sizes grow). In larger environments, the firing rates remain approximately the same, while field sizes cover the range $50 \lesssim D_g \lesssim 120$ cm, driving $\bar{\lambda}_g$ to even higher values (Brun et al., 2008). Thus, if the rat spends 2 to 3 seconds within a field, the expected firing probability,

$$\bar{p}_v^g = 1 - e^{-\bar{\lambda}_g},$$

is high—the corresponding cell fires almost certainly. In particular, the mean vertex opening probability exceeds the critical value p_v^*, which suggests that vertex percolation may indeed take place in the parahippocampal network. The expected probability of opening an edge e can be estimated from

$$\bar{p}_e^g = \bar{q}_e^g (\bar{p}_v^g)^2,$$

where $\bar{q}_e^g$ is the mean probability of reaching a grid field starting from its closest neighbor. Geometrically, $\bar{q}_e^g$ depends primarily on the lattice parameter ξ_g (see section 3). For the experimentally observed $\xi_g \approx 2/3$, the estimated value is about $\bar{q}_e^g(2/3) \approx 0.6$, which, for high enough $\bar{p}_v^g$, reaffirms the possibility that some grid cells may be systematically percolated during navigation.

2.2 Grid Field Percolation. These hypotheses can be tested by simulating a rat's navigation in triangular environments, for a set of spiking parameters. Experimentally, grid spacings a_g range along the ventro-dorsal axis of MEC from 0.3 m to 1.2 m in smaller environments (Stensola et al., 2012; Hafting et al., 2005) and from 1.7 m to 3 m and higher in larger environments (Brun et al., 2008). The place field sizes grow accordingly, and since the effect of speed is stronger for smaller fields, percolation is least likely to occur in smaller lattices.

For conservative estimates, the grid cell spacing was fixed at a lower value, $a_g = 60$ cm, while the lattice parameter varied from $\xi_g = 1/3$ to $\xi_g = 0.8$ (fields almost abut). The spatial phases and orientations of the grid field lattices $V_{\mathcal{E}}^g$ were randomized to represent different possibilities for cells sampled along the ventro-dorsal axis of MEC. To maintain realistic dynamics of spiking activity, the trajectories were generated by reshaping experimentally recorded paths in open arenas, preserving the observed speed of the animal. The length of each trajectory allowed producing at least 100 path segments extending from one side of the environment to another.

The results show that paths crossing an equilateral triangular enclosure with side $L = 6$ m start percolating grid cells as the lattice parameter and the firing amplitude exceed, respectively, $\xi_g \approx 0.6$ and $A_g \gtrsim 20$–25 Hz, independently from the lattice's shift and planar orientations (see Figures 2A and 2B). As ξ_g grows further, percolating paths start appearing at lower firing rates and quickly proliferate, densely covering the navigated area. Increasing A_g allows inducing percolation at lower ξ_g. The pairs (ξ_g, A_g) for which the percolation becomes possible form a boundary that separates "percolation phase" from the phase in which percolation is statistically suppressed (see Figure 2B).

Furthermore, once emerged, percolation becomes manifested at large scales, for example, in triangular domains that differ in size by an order of magnitude (see Figure 3A). The effect is strengthened as the cell's firing amplitude A_g grows, in a manner suggestive of a second-order phase transition controlled by two order parameters, ξ_g and A_g (Watanabe & Usui, 1985; Stokes & Hatch, 1991).

Note, however, that since higher firing rates are energetically costly, physiological magnitudes A_g should remain close to minimal values that permit a suitable percolation level at a given spatial scale. As shown on Figure 2B, these estimates are in agreement with the experimental data, which indicate biological viability of the percolation model.
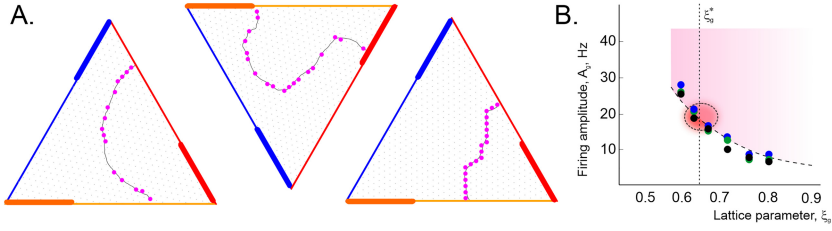
Figure 2: Grid field percolation. (A) A segment of simulated trajectory (gray line) passing through a large 20 × 20 m triangular environment. Active vertices are marked by pink circles. The first two paths are nonpercolating, and the third path percolates the enclosure. Side bars indicate $L/3$ length scale. (B) For a given set of parameters (ξ_g, A_g), the onset of the percolation phase was scored when at least 90% of grid cells were percolated by at least 5% of cross-environment path segments, and 90% of paths extending over at least $L/3$ percolate a grid cell. The latter condition defined the size of the simulated grid cell ensemble—about $N_g \gtrsim 200$ cells. Dots of different colors mark values obtained using different exploratory trajectories that cover the environment evenly, without artificially favoring one part of the environment over the other. The dashed line separates two phases of the grid cell network's activity: the pairs of (ξ_g, A_g)-values on its right (pink area) induce percolation, while the values on its left do not. The encircled area marks the domain of smallest A_g that permit percolation at $\xi_g \approx \xi_g^*$.
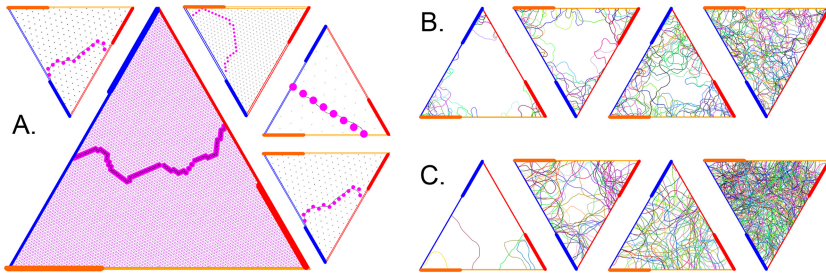

Figure 3: Scaling. (A) As the lattice parameter exceeds $\xi_g \approx 2/3$, percolating paths begin to appear at all scales. Shown are triangular environments with side lengths $L = 6$ m, $L = 12$ m, $L = 20$ m, and $L = 60$ m, along with a percolating path example. (B) As the rate A_g increases from 20 Hz to 200 Hz ($L = 12$ m, $\xi_g \approx 2/3$), larger parts of the environment become percolated. (C) Increasing ξ_g from 2/3 to 0.8 ($L = 20$ m, $A_g \approx 25$ Hz) boosts the percolation. Shown are path segments percolating the same cell, each shown with its own color. Side bars indicate $L/3$ length scale.

2.3 Spike Lattice in the Cognitive Map. The results discussed above were obtained by modeling the rat's moves through the firing fields in the observed environment—an approach that helps visualizing the grid cells' spiking patterns but may not directly capture the organization of the underlying network computations (Dabaghian et al., 2012; Dabaghian, 2021). Understanding the latter requires placing the grid cells' activity into the context of the brain's own representation of the environment—the cognitive map, encoded, inter alia, by the place cell and the head direction cell networks (Moser & Kropff, 2008; Grieves & Jeffery, 2017). The computational units enabling this representation are the functionally interconnected groups of hippocampal place cells, c_i (Harris, 2005; Dragoi & Buzsáki, 2006),

$$\sigma_i = [c_{i_0}, c_{i_1}, \ldots, c_{i_n}], \tag{2.4σ}$$

and head direction cells, h_i (Peyrache et al., 2015; Brandon et al., 2013),

$$\eta_j = [h_{j_1}, h_{j_2}, \ldots, h_{j_n}]. \tag{2.4η}$$

As their constituent place and head direction cells, the assemblies (see equation 2.4) are spatially selective and highlight, respectively, basic locations υ_{σ_i} and angular domains υ_{η_j} (Dragoi & Buzsáki, 2006; Harris, 2005; Peyrache et al., 2015; Brandon et al., 2013). The relative arrangement of these "fields" defines the order in which the assemblies ignite; knowing the latter allows decoding the animal's positions during active behavior (Jensen & Lisman, 2000; Frank et al., 2000; Guger et. al., 2011) and during the "off-line" memory explorations (Karlsson & Frank, 2009; Johnson & Redish, 2007; Dragoi & Tonegawa, 2011; Pfeiffer & Foster, 2013). One can hence model hippocampal representation of the grid cells' firing patterns by the same principle: each individual grid field υ_i^g is encoded by those place cell assemblies, $\sigma_{i_1}, \sigma_{i_2}, \ldots, \sigma_{i_k}$, whose fields are contained in υ_i^g, that is, by the place cells that exhibit coactivity with a given cell g and each other.

Computationally, the assemblies (see equation 2.4) are commonly modeled as the cliques of a graph that represents recurrent functional connectivity in the network, for example, of the *cognitive graph* that represents the collaterals in the CA3 region of the hippocampus (Muller et al., 1996; Burgess & O'Keefe, 1996). Simulations show that such assemblies form agglomerates, $\hat{\sigma}_i = \{\sigma_{i_1}, \sigma_{i_2}, \ldots, \sigma_{i_k}\}$, whose joint firing domains, $\upsilon_{\hat{\sigma}_i} = \upsilon_{\sigma_{i_1}} \cup \upsilon_{\sigma_{i_2}} \cup \ldots \cup \upsilon_{\sigma_{i_k}}$, cover the corresponding grid fields, υ_i^g. The resulting combinations of place and grid cells can hence be viewed as the units encoding the *spiking vertices*,

$$\hat{v}_i^g = [\hat{\sigma}_i, g], \tag{2.5}$$

in the hippocampal cognitive map.

The hexagonal order on these vertices is then established by concomitant activity of head direction assemblies from six "preferred" groups,

$$\mathfrak{h}^g = \{\hat{\eta}_1^g, \hat{\eta}_2^g, \ldots, \hat{\eta}_6^g\},$$

that activate on the runs between pairs of neighboring grid fields; for example, assemblies from $\hat{\eta}_1^g$ may activate when the rat runs approximately from left to right, assemblies from $\hat{\eta}_2^g$ then become active on the runs oriented 60 degrees from the left-right direction, and so forth (Peyrache et al., 2015). Correspondingly, the activity of η-assemblies from a particular $\hat{\eta}$-group that leads from a vertex $\hat{v}_i$ to a neighboring vertex $\hat{v}_j$ defines a *spiking edge*,

$$\epsilon_{i,j|k}^g = \{\hat{\sigma}_i, \hat{\sigma}_j | \hat{\eta}_k, g\}. \tag{2.6}$$

Together, the vertices (see equation 2.5) and the edges (see equation 2.6) define segments of a *spiking lattice* $\mathcal{V}_g$ embedded into the cognitive map. In the following, the superscript g and subscript k will be used to distinguish contributions from different grid and head direction cells and suppressed otherwise.

2.4 Percolation of Spiking Lattice. The "intrinsic" definition of the lattice elements (see equations 2.5 and 2.6) given above leads to a natural generalization of the grid field percolation model. As the animal's trajectory γ traverses a discrete sequence of σ-fields,

$$\Upsilon = \{v_{\sigma_1}, v_{\sigma_2}, \ldots v_{\sigma_n}, \ldots\},$$

a "firing tracer" of ignited place cell assemblies,

$$F_\sigma(\gamma) \equiv (\sigma_1, \sigma_2, \ldots), \tag{2.6σ}$$

is induced in the hippocampal network, along with a sequence of ignited head direction assemblies,

$$F_\eta(\gamma) \equiv (\eta_1, \eta_2, \ldots). \tag{2.6η}$$

The representation (see equation 2.6σ) of the navigated path (Jensen & Lisman, 2000; Frank et al., 2000; Guger et al., 2011) then allows defining *spiking percolation* as follows:

P1. A spiking vertex $\hat{v}_i$ *opens* when its constituent cells activate, that is, when a place cell assembly from its "hippocampal base" $\hat{\sigma}_i$ coactivates with the grid cell g.

P2. Two consecutively opening, neighboring vertices $\hat{v}_1$ and $\hat{v}_2$ produce an *open spiking edge* in $\mathcal{V}_{\mathcal{E}}$ if the head direction assemblies from a fixed group $\hat{\eta}_*$ remain active on the run from $\hat{\sigma}_1$ to $\hat{\sigma}_2$.

P3. The tracer $F_\sigma(\gamma)$ percolates through $\mathcal{V}_{\mathcal{E}}$ if it runs through a sequence of consecutively opening vertices $\hat{v}_i$ without omissions.

The grid field percolation discussed in section 2.2 can be viewed as a geometric, pictorial representation of the spiking percolation if the observed animal moves and the patterns of grid fields are physiologically actualized, that is, if place cells' activity marks every location of the rat and if the head direction activity chaperones every move between neighboring grid fields.[2] Simulations show that the required output is provided by as few as $N_c \gtrsim 100$ active place cells per unit area (1 m × 1 m; experimentally observed numbers are higher by an order of magnitude (Buzsáki, 2010)), with typical firing parameters (mean place field size $D_c \approx 24$ cm, and mean firing rate amplitudes $A_c \approx 20$ Hz). Furthermore, $N_h \gtrsim 60$ head direction cells firing with the amplitude $A_h \approx 20$ Hz over $D_h = 20°$ fields form lattice direction groups $\hat{\eta}_i$ (about 10 cells each) that distinguish runs of the simulated rat between different pairs of neighboring grid fields, which demonstrates that spiking percolation can occur within the physiological range of parameters. The resulting series of conjoint open spike edges,

$$\mathfrak{G}_g(\gamma) = \{\epsilon^g_{i_1 i_2}, \epsilon^g_{i_2 i_3}, \dots, \epsilon^g_{v_{i-1} i_k}\},$$

forms an intrinsic, spike-lattice representation of the grid field lattice path (see equation 1.1) at the scale defined by the lattice constant a_g.

2.5 Path Integration. A number of models were built to explain the role of the grid cells in the animal's capacity to optimize navigation using a cognitive map of ambient environment (Savelli & Knierim, 2019; Valerio & Taube, 2012; McNaughton et al., 2006). The mechanisms by which parahippocampal and entorhinal networks learn to represent space and retrieve the obtained information through autonomous network dynamics remain debated (Samsonovich & McNaughton, 1997; Valerio & Taube, 2012; McNaughton et al., 1996). A model suggested in Hasselmo (2008a, 2008b) implements the required hippocampal replays using persistently firing head direction cells that drive grid cells' firing from vertex to vertex, which in turn activate the corresponding place cell assemblies in spatial order. If the network is trained according to the coactivity between different types of neurons along the navigated path, for example, $\delta W_{\eta,\sigma} \propto \sum_i \vec{p}_{\eta_i} \vec{p}_{\sigma_i}$, where $\vec{p}_\eta$ and $\vec{p}_\sigma$ are the population activity vectors, then the learned

---

[2]To simplify modeling, movement direction was used as a proxy for the head direction, although physiologically, these parameters are not identical (Raudies et al., 2015; Dabaghian, 2022).

patterns can be reproduced autonomously in the retrieval phase. For example, head direction firing can be induced by the place cells that start spiking at a position σ,

$$\vec{p}_\eta = \sum_\sigma W_{\eta,\sigma} \vec{p}_\sigma, \tag{2.7}$$

which can then drive the grid cell membrane oscillations, thus generating hippocampal activity at the net step and so forth Hasselmo (2008a, 2008b).

From the perspective of this discussion, the network should be trained on the percolating paths only, which can then be reproduced during replays. Also note that consecutive activation of two hippocampal assemblies σ and σ' induced by a persistently firing head direction group η may be viewed geometrically as a transition of activity between two adjacent σ-locations aligned along the η-direction (Dabaghian, 2022). The Hasselmo model Hasselmo (2008a, 2008b) is hence based on using persistent head direction firing to guide place cell activity from a grid vertex to a neighboring one. As it turns out, this mechanism can be generalized to implement the transitions not only along the learned lattice edges but also to probe their vicinities, which significantly extends the scope of the model.

Consider an edge $\epsilon_{i,i+1|k}$ linking two open vertices, v_i and v_{i+1}, along a spike lattice direction $\hat{\eta}_k$. Let $T_{\hat{\eta}_l \hat{\eta}_k}$ be the matrix permuting the assemblies from two lattice direction groups, $\hat{\eta}_k$ and $\hat{\eta}_l$ (Means et al., 2020). Then the adjusted weight matrix,

$$T_{\hat{\eta}_l \hat{\eta}_k}(\sigma) W_{\hat{\eta}_k,\sigma} = W_{\hat{\eta}_l,\sigma}, \tag{2.8}$$

applied at the location σ in equation 2.7, redirects the persistent head direction activity from $\hat{\eta}_i$ to $\hat{\eta}_j$ (physiologically, this operation may be interpreted as, for example, a cortical or thalamic switch (Rikhye et al., 2018)). Two transformations of the weight matrices, equation 2.8 applied at the ends of an open edge $\epsilon_{i,i+1|k}$,

$$T_{\hat{\eta}_l \hat{\eta}_k}(\sigma_i) W_{\hat{\eta}_k,\sigma_i} + T_{\hat{\eta}_{l'} \hat{\eta}_k}(\sigma_{i+1}) W_{\hat{\eta}_k,\sigma_{i+1}} = W_{\eta,\dot{\sigma}_i}, \tag{2.9}$$

yield the weight matrix that funnels the activity from v_i and v_{i+1} to a side vertex, $\dot{v}_i$ (see Figure 4A). The same mechanism can then reroute the activity from the next open edge, $\epsilon_{i+1,i+2}$, to its side vertex $\dot{v}_{i+1}$, and so forth.

From the percolation model's perspective, activation of the side vertices also opens the edges that lead to these vertices, which geometrically amounts to "indenting" the percolated lattice paths (see Figure 4). A series of such indentations can deform and shift the representation of the original path over the spike lattice, $\mathfrak{G}_g \rightarrow \mathfrak{G}_g' \rightarrow \ldots \rightarrow \mathfrak{G}_g^{(k)} \rightarrow \ldots$, inducing geometrically deformed lattice paths that can generate hippocampal replays of
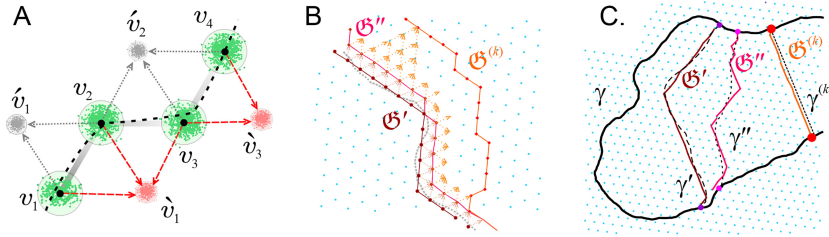
Figure 4: Path deformation. (A) The activity can transition from an open edge $\epsilon_{1,2}$ connecting two vertices v_1 and v_2 to its side vertex $\grave{v}_1$ (red field), thus opening the edges $\epsilon_{1,\grave{1}}$ and $\epsilon_{2,\grave{1}}$. Next, the activity can propagate from the adjacent open edge, $\epsilon_{2,3}$, to the side vertex $\grave{v}_2 = \grave{v}_1$, opening the edge $\epsilon_{3,\grave{1}}$, and so forth. The induced shifts are driven toward one side of $\mathfrak{G}$, to allow continuous attractor dynamics. The dashed curve represents a segment of the rat's trajectory. (B) A series of transformations (see equation 2.9) can be used to deform the percolating path $\mathfrak{G}_0$ over the lattice, $\mathfrak{G} \to \to \dots$ (C) Consecutive deformations of discretized paths (e.g., $\mathfrak{G}'$, $\mathfrak{G}''$) can be used to propagate replays of alternative trajectories (γ', γ'' e.g.) along the lattice and to produce lattice geodesics, the shortest paths between lattice vertices, such as $\gamma^{(k)}$.

alternative, "virtual" trajectories and thus guide spatial exploration (see Figure 4B; Sanders et al., 2015).

In particular, the possibility of deforming generic percolating paths allows establishing *lattice geodesics*—shortest chains of edges connecting pairs of vertices. Hippocampal replay of the shortest path between the underlying spatial locations σ and σ' may account, for the animal's ability to run from its current position straight to the nest, which is a key manifestation of path integration (Maaswinkel et al., 1999). Another implication is that the shortest paths across the spiking lattice define a global spatial metric— the discrete-geodesic distances between pairs of locations (Moser & Moser, 2008; see Figure 4C).

Note that the transformations (see equation 2.9) can be used to redirect the activity to both sides of the open edge series (see Figure 4A). However, if the head direction cells' firing is to form a single "activity bump" defining a compact range of angles (Bassett et al., 2018; Stringer et al., 2002), then the activity should be driven to one side of the percolated path $\mathfrak{G}_g$ only. Gradual shifts of the activity bump in the head direction network along a deformed path $\mathfrak{G}_g$ are then consistent with continuous reorientations of the animal's head.

3 Discussion

Grid cell activity is commonly studied from the perspective of extracting position codes and spatial metrics from the combinatorics of ad hoc

defined grid field indexes (Bush et al., 2015). Most models rely, tacitly or explicitly, on the assumption that a generic grid cell readily conveys spatial regularity of the grid field layouts to downstream networks through spiking outputs, over each navigated path. However, direct simulations show that over a given traveled route γ, most grid cells exhibit irregular spiking patterns that reflect the sequence in which their firing fields were visited rather than the abstracted order of the fields' spatial layout. The lattice-like structure of the latter is captured only by those cells, $\{g_1, g_2, \ldots, g_k\}_\gamma \equiv g_\gamma$, whose grids were percolated by γ and have therefore produced representations, $\mathfrak{G}_{g_1}(\gamma), \mathfrak{G}_{g_2}(\gamma), \ldots, \mathfrak{G}_{g_n}(\gamma)$, of γ in their respective spiking lattices, $\mathcal{V}_\mathcal{E}^{g_1}, \mathcal{V}_\mathcal{E}^{g_2}, \ldots, \mathcal{V}_\mathcal{E}^{g_k}$. The next path segment, γ', is represented by another percolated group $g_{\gamma'}$ that overlaps with $g_{\gamma'}$ and soon. The resulting series of overlapping percolated assemblies forms a grid cell firing tracer,

$$F_g \equiv (g_\gamma, g_{\gamma'}, \ldots),$$

that persistently drives hippocampal activity and allows representing longer, composite paths $[\gamma + \gamma' + \ldots]$. Note that from the point of view of grid cells' operability, the segments $\gamma, \gamma' \ldots$ may overlap and do not necessarily have to extend across the entire environment—these assumptions were made above for ease of presentation.

A compact bump of persistent head direction activity can then produce congruous deformations of the percolated path (see equation 2.9) in each contributing lattice, thus generating a compact continuous attractor activity in the hippocampal network (Romani & Tsodyks, 2010). This mechanism allows learning and replaying not only the actual percolating paths but also their deformations, thus establishing qualitative equivalences between discretized trajectories over spiking lattices, facilitating spatial learning, enabling path integration, and defining a global spatial metric of the encoded environment (Sanders et al., 2015).

According to the model, the grid cells' percolation onset is modulated by the shape of the navigated arena, but it is controlled primarily by several coupled physiological parameters—firing rates, field sizes, lattice spacings, rats' moves, and so forth (Watanabe & Usui, 1985). Additional restrictions may be required for proper coupling between different cell types (e.g., place field sizes should allow separating grid fields from each other) for encoding distinct vertices of the spiking lattice $\mathcal{V}_\mathcal{E}$. The full set of conditions defines a *percolation domain* $\mathcal{P}$ in the parameter space, analogous to the learning region $\mathcal{L}$ of parameters required for constructing topologically correct cognitive map from place cell activity (Dabaghian et al., 2012; Dabaghian, 2021). An implication of the model is that the experimentally observed spiking characteristics should fall into $\mathcal{P}$ and allow producing percolating paths in the amounts required for spatial information processing. Certain values can be localized with higher specificity; for example, the model predicts that the lattice parameter ξ_g should be attuned to the experimentally observed

magnitude $\xi_g^* \approx 2/3$ and points at the correct firing rate $A_g \approx 20\text{–}25$ Hz in smaller environments (Moser & Kropff, 2008; Hafting et al., 2005; Bush et al., 2015; Moser & Moser, 2008). Furthermore, the results point out that changes in one parameter may cause compensatory responses in others; for example, the network may lower firing rates as ξ_g grows, while producing longer percolating paths at a given lattice scale a_g may require increasing A_g or using larger fields, shifting the grid cell population activity along the ventro-dorsal axis of MEC.

Appendix: Geometric Estimates

Simulated trajectories were obtained by reshaping the recorded rat paths and embedding them into simulated environments—triangular enclosures of sizes $L = 6$ m, $L = 12$ m, $L = 20$ m, and $L = 60$ m (see Figure 2). The starting position was selected at the boundary of the enclosure randomly, with the velocity directed inward. The trajectory was then generated by time-integrating an experimentally recorded speed series and directing the velocity vector from one wall to another, with random instantaneous deflections distributed over an angular domain $[-\alpha, \alpha]$. The parameter α effectively controls the shape of the trajectory: small αs straighten the paths, and larger αs allow more "swirling" curves.

A.1 Site Opening Probability. The Poisson firing rate of a grid cell g is a function of the rat's position $\vec{r} = (x, y)$,

$$\lambda_g(\vec{r}) = \sum_i A_g e^{-\frac{|\vec{r} - \vec{r}_i^g|^2}{2\sigma_g^2}},$$

where A_g is the firing amplitude and σ_g defines the size of the firing field υ_i^g centered at the point $\vec{r}_i^g$. A path segment crossing through υ_i^g can be approximated by a chord of length l, parameterized by the variable u and positioned at the distance $l_\perp$ from the center (see Figures 5A and B). The mean integrated rate of the cell g is then

$$\bar{\lambda}_g = \int_{\bar{t}_g} \lambda_g dt \approx A_g \int_{AB} e^{-\frac{u^2 + l_\perp^2}{2\sigma_g^2}} \frac{du}{\bar{s}} = \frac{A_g}{\bar{s}} e^{-\frac{l_\perp^2}{2\sigma_g^2}} \int_{-l/2}^{l/2} e^{-\frac{u^2}{2\sigma_g^2}} du.$$

Using $D_g \approx 2\pi\sigma_g$ for the firing field diameter and the relationship $l_\perp^2 = D_g^2/4 - l^2/4$ yields

$$\bar{\lambda}_g = \frac{A_g D_g}{\sqrt{2\pi}\bar{s}} e^{-\frac{\pi^2}{2}} e^{\frac{\pi^2 l^2}{2D_g^2}} \operatorname{erf}\left(\frac{\pi l}{\sqrt{2}D_g}\right).$$
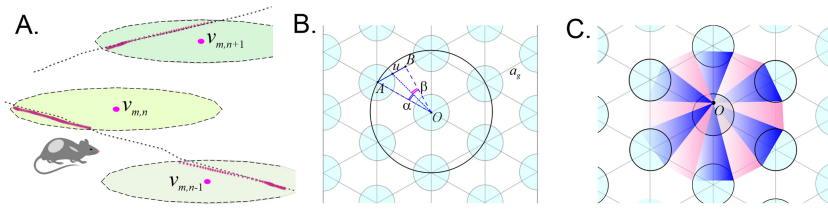
Figure 5: Grid cells. (A) A segment of the rat's trajectory can be approximated by a chord cutting through the grid fields. The right panel shows a chord AB of length l passing at the distance $l_\perp$ from the firing field center, v. (B) The vertex centered at A may open if the rat moves within the angular domain α (shaded blue); if the rat is directed within the domain β (shaded pink shade), then the trajectory escapes. (C) The geometry of the escape changes as the starting point O shifts, leading to small corrections to the probability estimate, proportional to the square of the distance between O and the field center.

From geometric probability theory, the average chord has length

$$\bar{l}_g = \pi D_g / 4$$

and hence passes at a distance $\bar{l}_\perp \approx 0.31 D_g$ from the field center (Kellerer, 1971), which allows writing

$$\bar{\lambda}_g = \frac{\bar{l}_g}{\bar{s}} A_g \left(\frac{2}{\pi}\right)^{3/2} e^{-\frac{\pi^2}{2}} e^{\alpha^2 \frac{l^2}{\bar{l}_g^2}} \operatorname{erf}\left(\alpha \frac{l}{\bar{l}_g}\right),$$

where $\alpha = \pi^2/(4\sqrt{2}) \approx \sqrt{3}$. The latter equation implies simply that the mean integrated rate is proportional to the mean time spent to run through the field, $\bar{t}_g = \bar{l}_g / \bar{s}$. The proportionality coefficient between $\bar{\lambda}_g$ and $\bar{t}_g$ can be interpreted as the characteristic rate during that run,

$$\bar{A}_g = A_g \left(\frac{2}{\pi}\right)^{3/2} e^{-\frac{\pi^2}{2}} e^{\alpha^2 \frac{l^2}{\bar{l}_g^2}} \operatorname{erf}\left(\alpha \frac{l}{\bar{l}_g}\right).$$

During an average run, for $l = \bar{l}_g$,

$$\bar{A}_g \approx 0.0755 A_g,$$

which is equivalent to equation 2.3. For example, if the maximal rate is $A_g = 25$ Hz, then $\bar{A}_g \approx 1.8$ Hz (similar values reported in Brun et al., 2008). If the mean speed is $\bar{s} = 10$ cm/sec and the mean field size is $D_g = 40$ cm, then $\bar{t}_g = \bar{l}_g / \bar{s} \approx 3$ sec and the net rate is $\bar{\lambda}_g \approx \bar{A}_g \bar{t}_g \approx 5.6$, that is, the cell spikes

with probability $\bar{p}_v^g \approx 99.6\%$). For $A_g = 10$ Hz, vertices open with probability $\bar{p}_v^g \approx 50\%$.

A.2 Bond Percolation Probability. Consider the case when the rat moves from the center v of a firing field, outward along a straight path. The probability p_b of reaching one of the neighboring fields is defined by the ratio of that field's angular size, as viewed from v, and the angular size of the gap between the firing fields (see Figure 5B). Due to symmetries, it is sufficient to consider the domain bounded by the angle $\angle(AOB)$ and the angles $\alpha \equiv \angle(AOu)$ and $\beta \equiv \angle(uOB)$, $\alpha + \beta = \frac{\pi}{6}$, which define the probability as

$$p_b = \frac{\alpha}{\alpha + \beta} = \frac{6\alpha}{\pi} = 1 - \frac{6\beta}{\pi}. \tag{A.1}$$

From the lattice's geometry, $|uB| = (a_g - 2R_g)/2$ and $|OB| = \sqrt{3}a_g/2$. From the triangle AOu, the distance $|Ou|$ is $|Ou|^2 = R_g^2 + a_g^2 - R_g a_g$, and from the triangle uOB, one has

$$|uB|^2 = |Ou|^2 + \frac{3}{4}a_g^2 - |Ou|a_g\sqrt{3}\cos\beta,$$

which yields

$$\cos\beta = \frac{\sqrt{3}a_g}{2\sqrt{R_g^2 + a_g^2 - R_g a_g}} = \frac{\sqrt{3}}{\sqrt{(\xi_g - 1)^2 + 3}}.$$

For small lattice parameter, $\xi_g \to 0$ (vanishing grid field size), $\beta \to \pi/6$, which eliminates the edge opening probability, $p_b(\pi/6) = 0$. Conversely, as the firing field size approaches the gap size, $\xi_g \to 1$, then the gap vanishes, $\beta \to 0$, which leads to the link opening, $p_b(0) = 1$. The physiological value $\xi_g^* \approx 2/3$ produces $\beta^* \approx 0.19$, which corresponds to an overcritical probability, $p_b(\beta^*) \approx 0.637$.

If the move starts with an offset Δr from the center of the firing field, $r = r_O + \Delta r$, then the escape probability (see equation A.1) will be an analytical function of $\Delta r/D_g \leq 1$. The zeroth-order term in the corresponding $(\Delta r/D_g)$-expansion is the mean probability given by equation A.1. The first-order term will vanish due to symmetries, and the nonvanishing corrections are therefore quadratic,

$$P_b(r) = P_b(r_O) + \partial^2 P_b(\Delta r/D_g)^2/2,$$

which justifies using equation A.1 for practical estimates.

Acknowledgments

References

Bassett, J., Wills, T., & Cacucci, F. (2018). Self-organized attractor dynamics in the developing head direction circuit. *Current Biology*, *28*(4), 609–615. 10.1016/j.cub.2018.01.010

Brandon, M., Bogaard, A., Schultheiss, N., & Hasselmo, M. (2013). Segregation of cortical head direction cell assemblies on alternating theta cycles. *Nature Neuroscience*, *16*, 739–748. 10.1038/nn.3383

Brun, V., Solstad, T., Kjelstrup, K., Fyhn, M., Witter, M., Moser, E., & Moser, M.-B. (2008). Progressive increase in grid scale from dorsal to ventral medial entorhinal cortex. *Hippocampus*, *18*(12), 1200–1212. 10.1002/hipo.20504

Burgess, N., & O'Keefe, J. (1996). Cognitive graphs, resistive grids, and the hippocampal representation of space. *Journal of General Physiology*, *107*, 659–662. 10.1085/jgp.107.6.659

Bush, D., Barry, C., Manson, D., & Burgess, N. (2015). Using grid cells for navigation. *Neuron*, *87*(3), 507–520. 10.1016/j.neuron.2015.07.006

Buzsáki, G. (2010). Neural syntax: Cell assemblies, synapsembles, and readers. *Neuron*, *68*, 362–385.

Coleman, R. (1969). Random paths through convex bodies. *Journal of Applied Probability 6*, 430–441.

Dabaghian, Y. (2021) From topological analyses to functional modeling: The case of hippocampus. *Frontiers in Computational Neuroscience*, *14*. 10.3389/fncom.2020.593166

Dabaghian, Y. (2022). Learning orientations: A discrete geometry model. *Journal of Applied and Computational Topology*, *6*, 193–220. 10.1007/s41468-021-00084-0

Dabaghian, Y., Mémoli, F., Frank, L., & Carlsson, G. (2012) A topological paradigm for hippocampal spatial map formation using persistent homology. *PLOS Computational Biology*, *8*, e1002581. 10.1371/journal.pcbi.1002581

Dragoi, G., & Buzsáki, G. (2006). Temporal encoding of place sequences by hippocampal cell assemblies. *Neuron*, *50*, 145–157. 10.1016/j.neuron.2006.02.023

Dragoi, G., & Tonegawa, S. (2011). Preplay of future place cell sequences by hippocampal cellular assemblies. *Nature*, *469*, 397–401. 10.1038/nature09633

Fiete, I., Burak, Y., & Brookings, T. (2008). What grid cells convey about rat location. *Journal of Neuroscience*, *28*(27), 6858–6871. 10.1523/JNEUROSCI.5684-07.2008

Frank, L., Brown, E., & Wilson, M. (2000). Trajectory encoding in the hippocampus and entorhinal cortex. *Neuron*, *27*(1), 169–178. 10.1016/S0896-6273(00)00018-0

Grieves, R., & Jeffery, K. (2017). The representation of space in the brain. *Behavioural Processes*, *135*, 113–131. 10.1016/j.beproc.2016.12.012

Grimmet, G. (1999). *Percolation*. Springer-Verlag.

Guger, C., Gener, T., Pennartz, C., Brotons-Mas, J., Edlinger, G., Bermúdez, I., . . . Sanchez-Vives, M. (2011). Real-time position reconstruction with hippocampal place cells. *Frontiers in Neuroscience*, *5*, 85. 10.3389/fnins.2011.00085

Hafting, T., Fyhn, M., Molden, S., Moser, M.-B., & Moser, E. I. (2005). Microstructure of a spatial map in the entorhinal cortex. *Nature*, *436*, 801–806. 10.1038/nature03721

Harris, A. (2005). Neural signatures of cell assembly organization. *Nature Reviews Neuroscience*, *6*, 399–407. 10.1038/nrn1669

Hasselmo, M. (2008a). Temporally structured replay of neural activity in a model of entorhinal cortex, hippocampus and postsubiculum. *European Journal of Neuroscience*, *28*(7), 1301–1315. 10.1111/j.1460-9568.2008.06437.x

Hasselmo, M. (2008b). Grid cell mechanisms and function: Contributions of entorhinal persistent spiking and phase resetting. *Hippocampus*, *18*(12), 1213–1229. 10.1002/hipo.20512

Jensen, O., & Lisman, J. (2000). Position reconstruction from an ensemble of hippocampal place cells: Contribution of theta phase coding. *Journal of Neurophysiology*, *83*, 2602–2609. 10.1152/jn.2000.83.5.2602

Johnson, A., & Redish, A. (2007). Neural ensembles in CA3 transiently encode paths forward of the animal at a decision point. *Journal of Neuroscience*, *27*, 12176–12189. 10.1523/JNEUROSCI.3761-07.2007

Karlsson, M., & Frank, L. (2009). Awake replay of remote experiences in the hippocampus. *Nature Neuroscience*, *12*, 913–918. 10.1038/nn.2344

Kellerer, A. (1971). Considerations on the random traversal of convex bodies and solutions for general cylinders. *Radiation Research*, *47*(2), 359–376. 10.2307/3573243

Kesten, H. (1982). *Percolation theory for mathematicians*. Birkhäuser.

Maaswinkel, H., Jarrard, L., & Whishaw, I. (1999). Hippocampectomized rats are impaired in homing by path integration. *Hippocampus*, *9*(5), 553–561. 10.1002/(SICI)1098-1063(1999)9:5⟨553::AID-HIPO9⟩3.0.CO;2-G

McNaughton, B., Barnes, C., Gerrard, J., Gothard, K., Jung, M., Knierim, J., . . . Weaver, K. (1996). Deciphering the hippocampal polyglot: The hippocampus as a path integration system. *Journal of Experimental Biology*, *199*(1), 173–185. 10.1242/jeb.199.1.173

McNaughton, B., Battaglia, F., Jensen, O., Moser, E., & Moser, M. (2006). Path integration and the neural basis of the "cognitive map." *Nature Reviews Neuroscience*, *7*(8), 663–678.

Means, S., Bläsche, C., & Laing, C. (2020). A permutation method for network assembly. *PLOS One*, *15*(10), e0240888. 10.1371/journal.pone.0240888

Moser, E., Kropff, E., & Moser, M.-B. (2008). Place cells, grid cells, and the brain's spatial representation system. *Annual Review of Neuroscience*, *31*(1), 69–89. 10.1146/annurev.neuro.31.061307.090723

Moser, E., & Moser, M.-B. (2008). A metric for space. *Hippocampus*, *18*(12), 1142–1156. 10.1002/hipo.20483

Muller, R., Stead, M., & Pach, J. (1996). The hippocampus as a cognitive graph. *Journal of General Physiology*, *107*, 663–694. 10.1085/jgp.107.6.663

Neher, T., Azizi, A., & Cheng, S. (2017). From grid cells to place cells with realistic field sizes. *PLOS One*, *12*(7), e0181618. 10.1371/journal.pone.0181618

Peyrache, A., Lacroix, M., Petersen, P., & Buzsáki, G. (2015). Internally organized mechanisms of the head direction sense. *Nature Neuroscience*, *18*, 569–575. 10.1038/nn.3968

Pfeiffer, B., & Foster, D. (2013). Hippocampal place-cell sequences depict future paths to remembered goals. *Nature*, *497*, 74–79. 10.1038/nature12112

Raudies, F., Brandon, M. P., Chapman, G. W., & Hasselmo, M. (2015). Head direction is coded more strongly than movement direction in a population of entorhinal neurons. *Brain Research*, *1621*, 355–367. 10.1016/j.brainres.2014.10.053

Rikhye, R., Gilra, A., & Halassa, M. (2018). Thalamic regulation of switching between cortical representations enables cognitive flexibility. *Nature Neuroscience*, *21*(12), 1753–1763. 10.1038/s41593-018-0269-z

Romani, S., & Tsodyks, M. (2010). Continuous attractors with morphed/correlated maps. *PLOS Computational Biology*, *6*(8), e1000869. 10.1371/journal.pcbi.1000869

Samsonovich, A., & McNaughton, B. (1997). Path integration and cognitive mapping in a continuous attractor neural network model. *Journal of Neuroscience*, *17*(15), 5900–5920. 10.1523/JNEUROSCI.17-15-05900.1997

Sanders, H., Rennó-Costa, C., Idiart, M., & Lisman, J. (2015). Grid cells and place cells: An integrated view of their navigational and memory function. *Trends in Neurosciences*, *38*(12), 763–775. 10.1016/j.tins.2015.10.004

Savelli, F., & Knierim, J. (2019). Origin and role of path integration in the cognitive representations of the hippocampus: Computational insights into open questions. *Journal of Experimental. Biology*, *222*, jeb188912. 10.1242/jeb.188912

Stensola, H., Stensola, T., Solstad, T., Froland, K., Moser, M.-B., & Moser, E. (2012). The entorhinal grid map is discretized. *Nature*, *492*, 72–78. 10.1038/nature11649

Stokes, H., & Hatch, D. (1991). Coupled order parameters in the Landau theory of phase transitions in solids. *Phase Transitions*, *34*(1–4), 53–67. 10.1080/01411599108205192

Stringer, S., Trappenberg, T., Rolls, E., & de Araujo, I. (2002). Self-organizing continuous attractor networks and path integration: One-dimensional models of head direction cells. *Network*, *13*(2), 217–242. 10.1080/net.13.2.217.242

Valerio, S., & Taube, J. (2012). Path integration: How the head direction signal maintains and corrects spatial orientation. *Nature Neuroscience*, *15*, 1445–1453. 10.1038/nn.3215

Watanabe, S., & Usui, T. (1985). Phase transition in coupled order parameter system. *Progress of Theoretical Physics*, *73*(6), 1305–1319. 10.1143/PTP.73.1305

Welinder, P., Burak, Y., & Fiete, I. (2008). Grid cells: The position code, neural network models of activity, and the problem of learning. *Hippocampus*, *18*(12), 1283–1300. 10.1002/hipo.20519

Wierman, J. (1981). Bond percolation on honeycomb and triangular lattices. *Advances in Applied Probability*, *13*(2), 298–313. 10.2307/1426685